International Journal of Multiphase Flow 141 (2021) 103678

Contents lists available at ScienceDirect

International Journal of Multiphase Flow

journal homepage: www.elsevier.com/locate/ijmulflow

# Clusters and coherent voids in particle-laden wake flow

Zhaoyu Shi [a], Fengjian Jiang [b,*], Lihao Zhao [c,a], Helge I Andersson [a]

[a] Department of Energy and Process Engineering, Norwegian University of Science and Technology, 7491 Trondheim, Norway
[b] Department of Ships and Ocean Structures, SINTEF Ocean, 7052 Trondheim, Norway
[c] AML, Department of Engineering Mechanics, Tsinghua University, 100084 Beijing, China

ARTICLE INFO

*Article history:*
Received 25 January 2021
Revised 10 April 2021
Accepted 26 April 2021
Available online 3 May 2021

*Keywords:*
Coherent voids
Smooth edges
Cylinder wake flow
Numerical simulation

ABSTRACT

Inertial point particles suspended in a two-dimensional unsteady circular cylinder flow at $Re = 100$ are studied by one-way coupled three-dimensional numerical simulations. The striking clustering pattern in the near-wake is strongly correlated with the periodically shed Kármán vortex cells. The particles are expelled from the vortex cores due to the centrifugal mechanism and coherent voids encompassing the local Kármán cells are therefore observed. The particle clustering at the upstream side of each void hole form a smooth edge, where the particle velocity magnitude is consistently lower than at the downstream edge of the voids. The trajectories of these particles originate from the side of the cylinder where the sign of vorticity is opposite to that of the vortex encompassed by the corresponding void hole. The particles are seen to decelerate along a substantial part of their trajectories. Particle inertia is parameterized by means of a Stokes number $Sk$ and smooth edges around the void holes still exist when $Sk$ is increased, although their formation is delayed due to larger inertia. Increasing inertia contributes to a decoupling of the particle acceleration from the slip velocity, which almost coincided at $Sk = 1$.



## 1. Introduction

Particle-laden flows around natural obstacles and man-made bluff bodies are frequently encountered in nature and industry. Even though the entering flow is regular and smooth, the fluid motion in the wake of the obstacle becomes more complex and comprises a variety of characteristic length and time scales. Insight in particle transportation and dispersion mechanisms in common bluff-body wakes may promote mitigation of industrial pollution and a better understanding of natural phenomena, such as scouring around offshore wind turbine foundations and clogging of steam generators in nuclear power plants at large scales, as well as enhancing the mixing performance of microfluidic reactors at small scales. Particularly, microfluidic systems are commonly applied in the lab-on-a-chip biological devices, wherein the flows are almost always laminar defined by a tiny pore scale. A number of experimental and numerical studies investigated the microparticle suspensions, e.g. particle migration and trapping in microchannels (Lee et al., 2010; Gijs et al., 2010; Dressaire and Sauret, 2017). The mixing or demixing processes can be manipulated with the fundamental insights of general particle-laden laminar vortex flows. The current understanding of the behavior of inertial particles even in the simplest bluff-body wakes is incomplete and no clue exists to how the remarkable particle clustering patterns arise.

Besides the occurrence of particle-laden wake flows in a variety of different settings, particle additives play a crucial role in dye and smoke flow visualizations. Cimbala et al. (1988) utilized a smoke-wire visualization technique to explore the wake formed behind a circular cylinder at relatively low Reynolds numbers. They aimed to investigate the far-wake behavior but realized that particles released from a smoke-wire retained a cellular pattern long after the characteristic Kármán vortices have largely diffused. This observation was interpreted as an inertia effect of particles since smoke in air is composed of tiny aerosol-type particles whose mass is significantly greater than the mass of the surrounding air molecules. The persistent smoke pattern showed that diffusion of smoke aerosols is extremely slow and the effective Schmidt number, i.e. the ratio of viscous diffusivity to the diffusivity of smoke particles in air, is orders of magnitude larger than unity. The tiny smoke particles do therefore not act as passive tracers and we believe that the effect of particle inertia can be understood in terms of a particle Stokes number rather than being lumped into an effective Schmidt number. The Stokes number ($Sk$) is adopted as a measure of particle inertia, typically defined as the ratio between the particle relaxation time $\tau_p$ and a characteristic time scale $\tau_f$ of the flow.

* Corresponding author.
*E-mail address:* Fengjian.Jiang@sintef.no (F. Jiang).

https://doi.org/10.1016/j.ijmultiphaseflow.2021.103678

The pioneering work by Jung et al. (1993) traced infinitesimal passive particles in an analytical two-dimensional (2D) wake flow behind a circular cylinder and analytically studied the importance of boundary conditions (BCs) to the particles' periodic orbits in the recirculation region. The follow-up study by Benczik et al., (2002) considered the motion of finite-size particles and manifested a sensitivity of inertia for particle trapping in a laminar cylinder wake flow. The seminal work by Tang et al. (1992) demonstrated patterns of rigid particle dispersion in a simulated mixing-layer and a plane wake. The behavior of these highly-organized particles, i.e. *particle clustering*, manifested a strong dependence on Stokes number and the large-scale flow structures (LSS) in a variety of configurations.

Experiments by Yang et al. (2000) showed snapshots of particle distributions for two different particle sizes, for which particles with $Sk$ of order unity were observed to present the most distinctive pattern. In another perturbation study with the Stokes drag force parameterized as a small disturbance, Burns et al. (1999) discussed the presence of a periodic attractor in a Kármán vortex street modeled as point vortices. The so-called dynamical attractor appeared as an indicator of particle focusing. Haller and Sapsis (2008) extended the scope to finite-size particles and constructed a slow manifold to describe the asymptotic attraction along trajectories of low-$Sk$ particles. Burger et al., (2006) compared the one-way and two-way coupled results in an oscillating hot-air circular cylinder wake flow at laminar condition by direct numerical simulations (DNSs). Afterwards, Yao et al. (2009) and Luo et al. (2009) also performed DNSs of a circular cylinder wake flow and presented clustering patterns in a better-resolved wake. The flow field exhibited vortices of different scales, determined by Reynolds number $Re$, which significantly affected the way of instantaneous particle clustering. A subsequent work (Zhou et al., 2011) additionally showed the temporal development of the particle distributions at a benchmarking $Re = 100$. Although the focus of Haugen and Kragset (2010) and more recent work by Aarnes et al. (2019) was on particle-cylinder impaction, glimpses of particle dispersion patterns in the near wake at $Re = 100$ were also presented.

Numerous efforts have been made in explorations of the underlying physical mechanisms of particle clustering, for instance in the paradigmatic homogeneous isotropic turbulence (HIT) and wall-bounded flows. The centrifugal effect induced by local vortices was recognized to interpret the tendency of particle clustering in strain-dominant regions (Squires and Eaton, 1991). This *strain-vorticity-selection* mechanism also applies in mixing-layers and shear flows (Eaton and Fessler, 1994). Previous numerical and experimental observations in HIT showed that the maximum clustering appeared at a Stokes number ($Sk_\eta$) based on the Kolmogorov time scale $\tau_\eta$ close to unity (Wang and Maxey, 1993; Aliseda et al., 2002; Salazar et al., 2008; Petersen et al., 2019).

The same optimal Stokes number for the maximum clustering was also reported for channel flow (Kulick et al., 1994) and wake flow behind a thick plane (Tang et al., 1992; Yang et al., 2000). The explanation of vortex ejection at the dissipative scales can also be extended to the inertial range and affected by self-similar multi-scale eddies (Yoshimoto and Goto, 2007; Bec et al., 2007). However, the centrifugal mechanism as the only effect fails for $Sk_\eta$ substantially larger than unity. Goto and Vassilicos (2008) proposed an alternative explanation for particles with moderate Stokes number, i.e. the *sweep-stick* mechanism. This process suggests that particles preferentially concentrate in regions with low fluid acceleration instead of low vorticity both in 2D and 3D (Coleman and Vassilicos, 2009). Additionally, Bragg and Collins, (2014) carefully compared other potential factors accounting for the cluster formation at a broad-scale spectrum, in which a statistical model (Zaichik and Alipchenkov, 2007) based on radial distribution functions (RDFs) in phase space emphasized the history effect of particle inertia along the trajectories. Bagheri and Sabzpooshani, (2020) recently investigated the role of history force on particle clustering in a 2D von Kármán flow and found the enhanced clustering at high $Sk$. Today it is commonly acknowledged that the centrifugal mechanism correlated to local flow structures is dominant up to $Sk \approx 1$, while other non-centrifugal mechanisms also have to be taken into account at higher Stokes numbers.

In contrast to the systematic investigations of particle clustering in HIT, little is known about the clustering mechanisms in *laminar* vortex-dominated flows, like for example the time-periodic Kármán vortex street and the time-evolving Taylor-Green vortex (TGV) flow. One may wonder whether the abovementioned mechanisms are acting also in these and other non-turbulent flows. Tang et al. (1992) proposed a stretching-folding mechanism, but only for mixing-layer flows, in which particles tend to aggregate in the thin regions outlining the boundaries of the LSS, regarded as stretching process. The folding process is related to the vortex pairing (Wen et al., 1992). This interpretation is still ambiguous and not applicable to cylinder wake flows. Raju and Meiburg (1997) indicated the action of centrifugal ejection in analytical models of a 2D solid-body vortex and a point vortex. The centrifugal force pointing outwards from the vortex core opposes other forces until an optimal ejection rate is reached. Candelier et al. (2004) highlighted another dissipative effect of the history force on particle trajectories which influenced the ejection rate in simple flows. Daitche and Tél (2011, 2014) improved the analysis in a modeled Kármán vortex flow and explicitly pointed out the suppression of concentration or attraction due to the history force for finite-size inertial particles (e.g. bubbles, oil droplets). However, these studies on clustering mechanisms are based on simplified and 2D flows, the explorations on real-life 3D vortex flows are still scarce. Recently, Jayaram et al. (2020) studied particle clustering in an evolving TGV flow and observed clustering in strain-rate dominated areas after the LSSs had been broken down to small-scale eddies so that an effective Stokes number, based on the viscous dissipation time scale, became of order unity.

To objectively characterize particle clustering, quantitative measurements of clustering have been escalated from box counting (Aliseda et al., 2002), correlation dimension (Tang et al., 1992; Bec et al., 2007), RDFs (Zaichik and Alipchenkov, 2007; Ireland et al., 2016) to Voronoï diagrams (Monchaux et al., 2010). The two latter ones are currently the most widely used approaches, of which a RDF is spatially-averaged for each manually selected length-scale and thus fails to provide information of individual clusters. By contrast, information about instantaneous local clustering is accessible via Voronoï diagrams for which the number of particles should be carefully chosen in terms of statistical analysis. A recent experimental HIT study by Petersen et al. (2019) found high consistency between the two approaches. Mohammadreza and Bragg (2020) extensively applied Voronoï cells to investigate the effects of $Re$ and gravity on clustering in HIT using DNS. Moreover, Shi et al. (2020) applied Voronoï diagrams to analyze a striking bow-shock clustering in the vicinity of a circular cylinder. Alternative dynamical techniques, such as finite-time Lyapunov exponents (Bec et al., 2006a; Jacobs and Armstrong, 2009; Daitche and Tél, 2014) and acceleration analysis (Bec et al., 2006b), which rely on particle trajectories, are mainly effective for particles with modest inertia, i.e. small Sk. Another approach is based on the application of an Eulerian velocity-acceleration structure function (Gibert et al., 2012), showing the tendency of clustering in high-strain regions. The review article by Monchaux et al. (2012) provides a comprehensive overview of the different techniques used to characterize particle clustering.

The motivation of the present study is to investigate clustering of heavy inertial particles in the near wake of a circular cylinder

flow at $Re = 100$. Of particular interest is to provide an in-depth exploration of a striking phenomenon, namely the formation of *coherent voids*, and how and why these voids are bounded by a *smooth edge* consisting of densely concentrated particles. This phenomenon is not a numerical artifact but a reality of practical interest, for instance with respect to homogenization of particle additives. The phenomenon has been observed before in some numerical simulation studies (Yao et al., 2009; Haugen and Kragset, 2010; Aarnes et al., 2019), but been left almost unnoticed and without being scrutinized. Therefore a couple of questions remain to be answered: why and how do particle clustering appear in a laminar Kármán vortex street? How do the characteristic coherent voids form and evolve in space and time? How are the particle structures correlated with the local vortices? These questions will be addressed in the present paper which can be considered as a sequel to the differently focused paper by Shi et al. (2020).

The paper is organized as follows: the mathematical problem, the simulation method and numerical details are first described in Section 2. Results for $Sk = 1$ particles are presented and discussed in three sub-sections. The traveling features of the coherent voids and their smooth edges are considered in sub-sections 3.1 and 3.2, respectively, whereas the key observations made from particle trajectories are addressed in 3.3, in terms of both group and individual trajectories. Finally, in order to elucidate the crucial role of particle inertia, comparisons of results obtained for some different Stokes numbers are made in Section 4, before conclusions are drawn in Section 5.

## 2. Problem formulation and numerical methods

### 2.1. Equations of motions

Three-dimensional numerical simulations of flow around a circular cylinder at Reynolds number $Re = U_0 D/\nu = 100$ (free stream velocity $U_0$, cylinder diameter $D$, kinematic viscosity $\nu$) are conducted using a well-verified DNS/LES solver called MGLET (Manhart et al., 2001; Manhart and Friedrich, 2002). We utilize a second-order finite-volume method to discretize the incompressible continuity and Navier-Stokes (N-S) equations. The transient flow is time-advanced by an explicit low-storage third-order Runge-Kutta scheme. The instantaneous fluid velocity components and pressure are preserved in discrete staggered equidistant cubic Cartesian grids. One-way coupling is deployed, i.e. the particle movement does not affect the underlying fluid velocity and particle-particle collision is neglected. The Poisson equation is iteratively solved by Stone's strongly implicit procedure. We exploit a cut-cell immersed boundary method (CCIBM) to exactly compute the shapes of polyhedron cells intersected by the curved cylinder wall. The normal vector of the intersected cells is obtained to define the particle-wall collision boundary condition.

The inertial particles laden in the unsteady laminar wake flow are modeled as point-like spheres with radius $a$ in a dilute suspension. The density ratio $\rho_p/\rho_f$ is taken as $10^3$ ($\rho_p, \rho_f$ are the densities of particle and fluid, respectively), and gravity is neglected since we only intend to investigate the inertial effect in this work. The individual particles are only under the effect of drag force

$$\boldsymbol{F} = 6\pi\mu a\beta[\boldsymbol{u}_{f@p} - \boldsymbol{u}_p(\boldsymbol{x}_p, t)], \tag{1}$$

which results from the *slip velocity* $\boldsymbol{U}_s = \boldsymbol{u}_{f@p} - \boldsymbol{u}_p(\boldsymbol{x}_p, t)$. Herein, $\boldsymbol{u}_{f@p}$ is the local fluid velocity at particle position $\boldsymbol{x}_p$. The empirical correction factor $\beta = C_D Re_p/24$ is unity in the Stokesian limit $Re_p = 0$, where $Re_p = 2a||\boldsymbol{u}_p - \boldsymbol{u}_{f@p}||/\nu$ is the particle Reynolds number. The modified finite-$Re_p$ drag coefficient $C_D$ is a function of $Re_p$ estimated as

$$C_D = \frac{24}{Re_p}(1 + 0.15Re_p^{0.687}) + \frac{0.42}{1 + 4.25\times 10^4 Re_p^{-1.16}} \tag{2}$$

**Table 1**
The average particle Reynolds number $\langle Re_p\rangle$ and peak value $Re_{p,m}$ for each $Sk$ at time $t^*$.

| $Sk$ | 1 | 3 | 5 | 8 | 12 | 16 |
|---|---|---|---|---|---|---|
| Average $\langle Re_p\rangle$ | 0.092 | 0.258 | 0.472 | 0.718 | 1.001 | 1.323 |
| Maximum $Re_{p,m}$ | 0.833 | 1.859 | 2.834 | 3.796 | 4.797 | 5.798 |

for $Re_p < 3\times 10^5$ (Cliff et al., 1978, Chapter 5). The empirical drag law Eq. (2) is well-justified under a steady uniform flow at moderate $Re_p$ (from 1 up to $10^3$) (Bagchi and Balachandar, 2003). From a practical perspective, Eq. (1) is also widespread in most known studies. The simplified Maxey-Riley (M-R) equations (Maxey and Riley, 1983) give us the Lagrangian particle information as such,

$$\boldsymbol{a}_p = \frac{d\boldsymbol{u}_p}{dt} = \frac{C_D Re_p}{24\tau_p}(\boldsymbol{u}_{f@p} - \boldsymbol{u}_p), \quad \frac{d\boldsymbol{x}_p}{dt} = \boldsymbol{u}_p. \tag{3}$$

where $\boldsymbol{a}_p$ is the particle acceleration. The particle velocity $\boldsymbol{u}_p$ is updated by an adaptive fourth-order Rosenbrock-Wanner scheme with a third-order error estimator (Gobert, 2010) and an explicit Euler scheme is used to update particle position $\boldsymbol{x}_p$. The particle equations are integrated forward in time with the same time step used in solving the N-S equations. The local fluid velocity components are obtained by a linear interpolation. A measure of particle inertia is defined as $Sk = \tau_p/\tau_f$, where $\tau_p = 2\rho_p a^2/9\rho_f\nu$ is the particle response time to changes in the local fluid velocity and $\tau_f = D/U_0$ denotes the nominal time scale of the flow field. An alternative timescale of the fluid field associated with Kármán vortices can be defined as the inverse of the maximum absolute spanwise vorticity, i.e. $\tau_{f\nu} = 1/|\omega_z|$. We believe that this vorticity-based time scale is physically more relevant than the time scale of the vortex shedding. An 'effective Stokes number' based on this vorticity-time scale is thus defined as $Sk_e = \tau_p/\tau_{f\nu} = |\omega_z|\tau_p$, where $|\omega_z|$ decays downstream. In other words, for such single dominating timescale flow, it is only a scaling matter whether to present the results with an effective or the nominal $Sk$ number and the observed physics are not going to be affected by the choice of timescale. Table 1 shows both the average and peak value of $Re_p$ obtained from samples within $[-0.5D, 15.8D]$ along streamwise X-direction. Nevertheless $Re_p$ increases as $Sk$ is larger, the maximum $Re_p$ is only 5.8 for all considered $Sk$-numbers computed from the relatively small slip velocity $\boldsymbol{U}_s$. This indicates the applicability of the finite-$Re_p$ correction in Eq. (2). Note that we adopt a 'sliding motion' collision model at the surface of the cylinder, wherein the particle wall-normal velocity reduces to zero while the wall-tangential velocity component preserves, details of which are reported in the recent work by Shi et al. (2020).

### 2.2. Computational details

We consider a cuboid box discretized by a multi-level structured Cartesian mesh, in each of which $N^3$ cubic cells are uniformly distributed. The range of the computational domain is $[-16.384D, 16.384D]$ in the streamwise X-direction, $[-8.192D, 8.192D]$ in the crossflow Y-direction and $[0, 4.096D]$ in the spanwise Z-direction. The center of the cylinder sits at (X=0, Y=0). A local grid refinement is enforced in the vicinity of the cylinder and the total number of grid points are around $1.65\times 10^7$ with a resolution of $\Delta_{\min}/D = 0.016$. The discrete N-S equations are integrated in time and space on this grid configuration. A periodic boundary condition is imposed in the homogeneous Z-direction. A constant free-stream velocity condition and Neumann condition on pressure $\partial p/\partial x = 0$ are applied at the inlet plane. The outlet BC contains zero pressure and $\partial u/\partial x = \partial v/\partial x = \partial w/\partial x = 0$. Free-slip BCs are enforced at the two side-walls normal to Y-direction, i.e. $v = 0$ and $\partial u/\partial y = \partial w/\partial y = 0$.

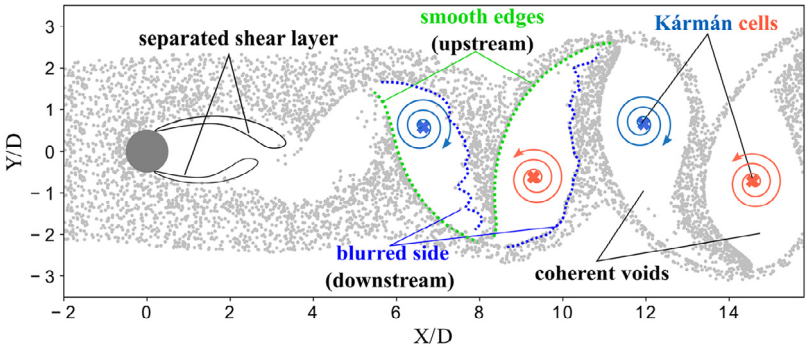


**Fig. 1.** (color online) Schematic of the instantaneous particle field with superimposed blue and red whirls illustrating oppositely rotating Kármán vortex cells. (For interpretation of the references to colour in this figure legend, the reader is referred to the web version of this article.)

**Table 2**
Particle simulation framework for each *Sk* in two groups.

| Case no. | Injected particle (Y/D)×(Z/D) number per timestep | Injection area | Sample region (X/D) | Sample number in total |
|---|---|---|---|---|
| 1 | 9 | (−4.096, 4.096)×(0, 2.048) | (−2.5, 15.8) | $4.7 \times 10^4$ |
| 2 | 2 | (−2.048, 2.048)×(0, 1.024) | (−2.5, 16.5) | $6.1 \times 10^3$ |

After running the simulation for $400\tau_f$, the unsteady flow has developed into a strictly periodic vortex shedding regime. The time-averaged drag coefficient $C_d = 2F_d/\rho_f U_0^2 LD$ and standard deviation of the lift-coefficient $C_{l-rms} = 2F_{l-rms}/\rho_f U_0^2 LD$ ($F_d$ drag force, $F_{l-rms}$ root-mean-square lift force, $L$ cylinder length) are obtained to be 1.391 and 0.240, respectively. The Strouhal number $St = f\tau_f$ is calculated as 0.168 via fast Fourier transformation (FFT). The measured parameters are all within the ranges reported by others, see Ferziger and Tseng (2003). In a post-processing step, we deduced the spanwise vorticity $\omega_z$ from the computed velocity components as $\omega_z = \partial v/\partial x - \partial u/\partial y$. The identification of a vortex employed here, according to the *Q-criterion* (Hunt et al., 1988), is a spatial region where the second invariant of the velocity gradient tensor $Q = \frac{1}{2}(|\boldsymbol{\Omega}|^2 - |\boldsymbol{S}|^2)$ is positive ($\boldsymbol{\Omega} = \frac{1}{2}[\nabla \boldsymbol{u} - (\nabla \boldsymbol{u})^T]$ and $\boldsymbol{S} = \frac{1}{2}[\nabla \boldsymbol{u} + (\nabla \boldsymbol{u})^T]$ are the rotation-rate tensor and strain-rate tensor, respectively).

Inertial particles are seeded into the flow from the inlet at initial velocity $U_0$. The particle simulation, starting at $400\tau_f$, lasts 8 vortex shedding periods (total number of timesteps 9448). At each timestep $i_{step} = 1, 2, \ldots, 9448$, a certain number of new particles are released into the flow and others are leaving the domain through the outlet. Fig. 1 shows the snapshot of the particle distribution and the extracted vortex cores from DNS data at the last timestep $i_{step} = 9448$. The terminology used afterwards are depicted along with the corresponding schematic topology.

Six different Stokes numbers are considered, i.e. $Sk = 1, 3, 5, 8, 12, 16$. Unlike the tracer particles approaching the cylinder wall without colliding, inertial particles lose part of their kinetic energy due to collision with the cylinder surface. We perform two groups of particle simulations with different seedings shown in Table 2. The first case serves for the purpose to exhibit the particle clustering with the sufficient samples used in Sec 3.1 and 3.2. In the second simulation, we intend to output the essential quantities along each particle trajectory at every timestep. The heavy dataset requires to reduce the number of injected particles, therefore, the injection area is only a quarter of that in the first simulation. In the post-processing, we only select the useful particle samples along the streamwise X-direction which are near the cylinder and involved with vortices in the wake. The total particle numbers of the two cases used for statistical analysis in Sec 3.3, are different by a factor of 8.

## 3. Results and discussion

### 3.1. Traveling of 'void holes'

The instantaneous particle concentration seen in Fig. 1 exhibits a peculiar repetitive pattern, which intuitively reflects the underlying Kármán vortex street. The characteristic concentration pattern of the $Sk = 1$ particles will be thoroughly explored in the next three sub-sections with focus on the formation and propagation of the void holes (empty areas). Before the closing of the paper, Stokes number effects will be addressed in Section 4. Since the flow at $Re = 100$ is two-dimensional and two-componential, i.e. the only two velocity components $u$ and $v$ are independent of Z, all particles are projected into a single XY-plane. Fig. 2 shows how void holes form in the shadow of the cylinder and travel downstream during one shedding period $T = D/(St \cdot U_0) \approx 6D/U_0$, starting at time $t^* \approx 47D/U_0$, i.e. about 8 shedding periods after the start of the particle seeding. Five leaf-shaped void holes, labeled from 0 to 4, can be seen in the uppermost panel at time $t^*$. Each of the void holes are partially overlapping with a local vortex cell, visualized by means of the spanwise vorticity $\omega_z$. Consecutive snapshots, separated $T/8$ in time, are shown in the subsequent plots, in which we focus on the motion and shape of hole no 1. The shape of the void hole is approximated by a leaf-shaped contour (in cyan) of which the centroid is indicated by a cross. We observe that the void hole translates downstream with negligible lateral excursions. The void hole becomes more upright with time, which represents a very modest clockwise rotation, i.e. in the same sense as the rotation of the underlying Kármán vortex. The upper part of the periphery of the hole becomes more rounded, whereas the lower cusp becomes peakier. The length of the perimeter of hole no 1 increases by ca 35% during the shedding period considered, thus reflecting the increasing area of the void. A possible void distortion likely caused by an insufficient blockage ratio $\alpha = L_y/D$ can thus be excluded in view of the almost proportional increase of perimeter and area. After a half shedding cycle the topology of the concentration pattern exhibits a mirror-symmetry with respect to the X-axis of that of the original pattern at $t^*$. After a complete shedding cycle $T$, the void hole no 1 has translated to the earlier position of void hole no 3, whereas void hole no -1 has taken over the original position of void hole no 1.

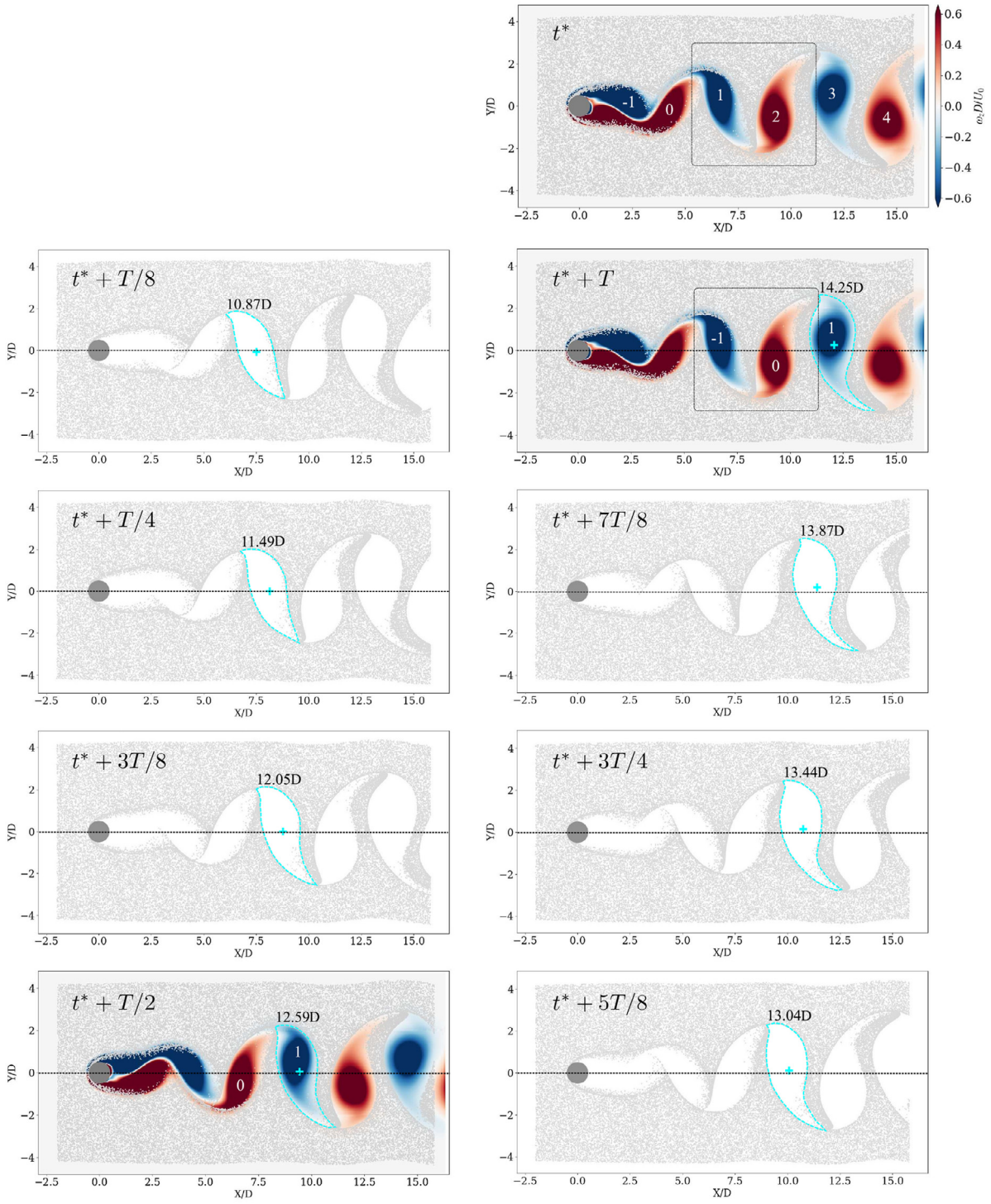


**Fig. 2.** (color online) Time-sequence of particle distributions during one vortex shedding period $T$. The characteristic snapshots of the clustering patterns of $Sk = 1$ particles are $T/8$ apart in time. The approximate outline and the centroid (+) of hole no 1 are colored in cyan and the perimeter is indicated at the top. The spanwise vorticity field $\omega_z D/U_0$ is superimposed on the particle distributions at time $t^*$, $t^* + T/2$ and $t^* + T$.

Let us now take a closer look at how the void holes travel in Fig. 3, where the fluid velocity field now is characterized by the scalar $Q$-field. The centers of Kármán vortices are marked by orange dots whose position is decided by the local maxima of $Q$, and the grey chunks represent fluid with $Q > 0$. Unlike the centroids of the void holes (black +), which translate downstream with negligible lateral excursions, the center of the anti-clockwise vortex associated with void hole no 0 is well below the Y-axis, whereas the center of the clockwise vortex cell corresponding to hole no 1 is above the symmetry plane. Although the void holes encompass the Kármán vortex cells, the centroid of a given hole does not coincide with the center of a Kármán vortex. This observation cannot readily be made from the Fig. 2. It is worth to note that the relative distance between the vortex core and the void centroid persists, i.e. that the vortex core remains most offset from the symmetry plane of the wake (Y=0). According to Fig. 3, however, the displacement

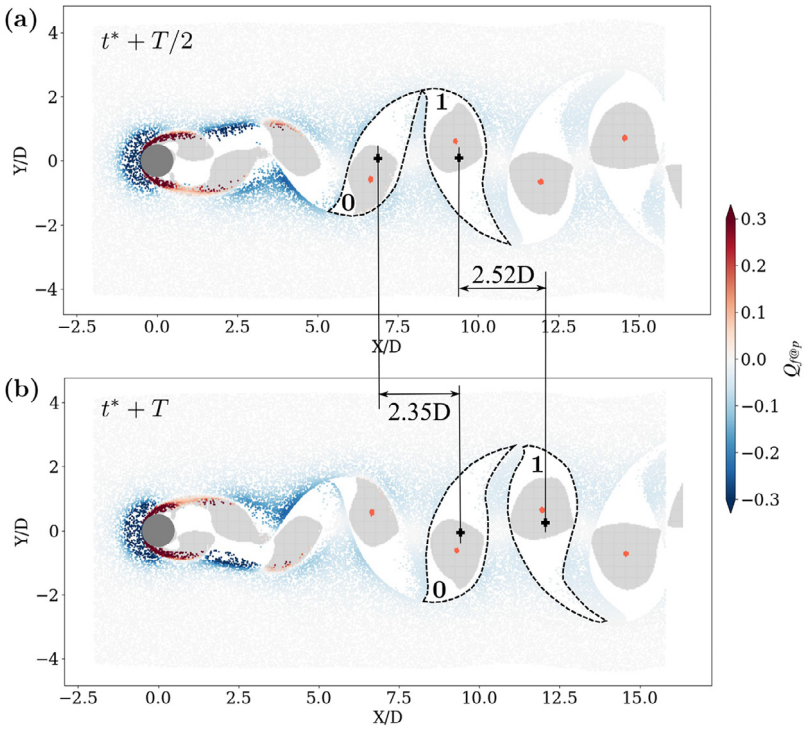


**Fig. 3.** (color online) Particle distributions and $Q$ at time (a) $t^* + T/2$ and (b) $t^* + T$. The $Sk = 1$ particles are colored by the local value of $Q$, i.e. $Q_{f@p}$. The grey chunks inside the void holes represent parts of the flow field with $Q > 0$ and the orange dots show positions of local maxima of $Q$. The translational distance of the centroids (+) of void holes no 0 and no 1 can be measured over the time interval $T/2$. The numbering of the void holes refers to the top panel in Fig. 2.

between the vortex core and the void centroid decreases in the downstream direction, ca 10.2% and 22.1% for void no 0 and no 1, respectively, despite that the displacement at upstream is larger than that at downstream. The reason for the displacement diminishing with time is likely to be attributed to the gradually changing shape of the voids, which shifts the centroids closer to the vortex cores whereas the upstream void hole expands at a slower rate.

The particles have been colored by local $Q$ at particle position, i.e. $Q_{f@p}$. The vast majority of the particles is bluish, which means that they are in a strain-rate dominated region characterized by negative $Q$-values. One can therefore infer that the $Sk = 1$ particles are expelled from the rotation-dominated Kármán vortex cells and swept to the borders of the void holes. However, it is surprising to observe the many reddish particles located in the two shear layers emanating from the surface of the cylinder. The centrifugal mechanism is active when an inertial particle tries to follow a curved trajectory whereas a particle in a separated shear layer follows a mildly curved path. That is why numerous particles can be seen in the shear layers, in spite of $Q$ being positive. Here, positive $Q_{f@p}$ implies that the rotation rate exceeds the strain rate.

By measuring the traveling distance of the centroids of void hole no 0 and hole no 1 over the time interval $0.5T$ between the two plots, the translational speed of the two holes can be estimated as $0.796U_0$ and $0.854U_0$. The higher speed of hole no 1 reflects the monotonically decreasing velocity deficit with downstream distance X. This reduction of the velocity deficit and the accompanying attenuation of the strength of the vortex cores contribute to the persistent shape of the void holes. The traveling speed of the holes seems to be consistent with the estimated speed $0.895U_0$ of the Kármán vortex cells. The slightly lower traveling speed of the holes can be ascribed to the inertia of the $Sk = 1$ particles. The wavelength $\lambda_x$, i.e. the distance between two successive vortex cores with the same sign of $\omega_z$, is about $5.284D$. These estimates of the vortex speed and separation are consistent with data reported from the DNS study by Mowlavi et al. (2016), albeit in presence of a somewhat insufficient blockage ratio in their computational set-up.

### 3.2. Tracking 'smooth edges'

An interesting phenomenon can be observed already from Fig. 2, namely that particles are densely clustered and form a smooth edge at the upstream side of the void holes. The particles are comparatively more dispersed around the downstream side of the void holes, and the edge of the hole is rather blurred near the cusp. Careful inspection of plots by others, notably (Yao et al., 2009; Haugen and Kragset, 2010) and (Aarnes et al., 2019), shows the same tendencies, but this peculiar phenomenon has neither been addressed nor explained before. To this end we introduce Voronoï diagrams in Fig. 4 to investigate the local particle concentration. The inverse of the area $A$ of a Voronoï cell is a measure of the particle concentration. The leaf-shaped void holes comprise Voronoï cells which are order-of-magnitudes larger than the surrounding Voronoï cells. This cell pattern resembles reticulated veins with the thinnest cell-shape at the upstream (left) half of the void hole. These needle-like Voronoï cells result from the densely populated smooth edge of the void hole.

The particles in Fig. 4 are colored by local $Q_{f@p}/A$ in order to emphasize particles around the void holes better than in Fig. 2. No particles downstream of X=5$D$ are seen to be in rotation-dominated ($Q > 0$) areas and the vast majority of the particles are in strain-dominated ($Q < 0$) areas. Particles near the center-plane ($Y = 0$) are greyish/white ($Q \approx 0$), i.e. neither affected by strain nor by rotation. Recall from Fig. 2 that the vorticity is negligible between the vortex cells and we can now infer that also the strain-rate is negligibly small in this area (between the wavy red-dashed lines).

How is the smooth edge of a void hole formed and maintained? Let us examine the history of the particles which form the smooth edge of holes no 3 and 4 at time $t^*$. The particles at the edge of

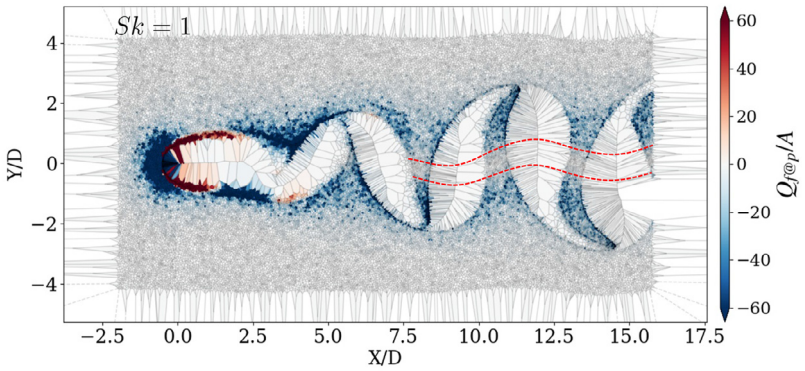


**Fig. 4.** (color online) Voronoï diagrams at time $t^*$. The $Sk = 1$ particles are colored by $Q_{f@p}/A$, where $A$ is the area of the corresponding Voronoï cell. $Q_{f@p}/A \approx 0$ in the white band between the two undulating dashed red lines. (For interpretation of the references to colour in this figure legend, the reader is referred to the web version of this article.)

hole no 3 are backtracked in time and plotted in Fig. 5(a) at four earlier time instants $T/4$ apart. The fast-moving particles that make up the smooth edge of void hole no 3 (encompassing a clockwise-rotating Kármán vortex) seem to stem from the smooth edge of hole no 1, which now resides at the earlier position of void hole no 3. The particles, especially those forming the upper part of the smooth edge, seem to translate collectively almost as an ensemble. These particles are not only traveling in the streamwise direction but also translate upwards. This excess traveling distance requires a higher particle velocity magnitude $|\boldsymbol{u}_p|$, as seen by the dark-red colored particles. We believe that the excess velocity is provided by the clockwise-rotating Kármán vortex, which tends to accelerate not only the fluid but also the particles in the upper half of the vortex cell. Similarly, the fast-moving particles that make up the smooth edge of void no 4 (characterized by anti-clockwise vorticity) in Fig. 5(b) seem to stem from the smooth edge of void hole no 2, which is where void no 4 happened to be one shedding period $T$ earlier. The particles that belong to the lower part of the smooth edge are deflected laterally, i.e. downwards, and accordingly move faster than the particles that belong to the upper part of the smooth edges and primarily translate in the X-direction. We are now able to choose a relevant vorticity strength connected with the property of smooth edges to define $Sk_e = |\omega_z|D/U_0 \cdot Sk$. The backtraces of a smooth edge shown in Fig. 5 verify that the expelled particles maintain their relative positions to the local vortex core during the convection once they undergo the most intensive centrifugal ejection around void 0 region. The vorticity maximum of the first detached vortex is thus reasonably used to define $Sk_e = 2.08Sk$, which also indicates a substantial inertial effect in accordance with the nominal $Sk$ equal to unity.

A further look at the particles already examined in Fig. 5(b) is taken in Fig. 6, which shows the magnitude and direction of the acceleration $\boldsymbol{a}_p$ of the particles that make up the smooth edge of void hole no 4 at time $t^*$. Already one shedding period earlier, when these particles resided around the upstream edge of the present-time hole no 2, only the particles clustered around the lower part of the smooth edge exhibited a substantial acceleration $|\boldsymbol{a}_p|$ with a distinct component in the positive Y-direction. This is consistent with the relatively high velocities $|\boldsymbol{u}_p|$ of particles at the smooth edge of hole no 4. The significant component of $\boldsymbol{a}_p$ perpendicular to $\boldsymbol{u}_p$ suggests that these particles are deflected upwards, i.e. towards the symmetry plane of the wake.

Contrary to Fig. 6, in which the particles were backtracked in time, Fig. 7 shows the acceleration $\boldsymbol{a}_p$ of all particles at the same instant of time $t^*$. The magnitude of the particle acceleration decays with streamwise distance (the color changes gradually from blue to green). Particularly strong accelerations are seen on both sides of the void holes and most notably near the center of the corresponding Kármán vortices. These accelerations are towards downstream at the smooth edge but upstream at the blurred downstream side of each void hole. The reason that the acceleration vectors roughly point to the center of the Kármán vortex cells is in order to make the particles follow a circular trajectory around the vortex cores (orange dot). The high $|\boldsymbol{a}_p|$ exhibits similar undulations about the mid-plane (Y=0) as the white band in Fig. 4.

The slip velocity vector $\boldsymbol{U}_s$ determines the drag force $\boldsymbol{F}$ in Eq. (1) and therefore also the particle acceleration $\boldsymbol{a}_p$ in Eq. (3). The streamwise and cross-stream components of $\boldsymbol{U}_s$ are shown in Fig. 8, where the streamwise component $U_{s,x}$ in Fig. 8(a) alternates between positive and negative values, whereas the cross-stream component $U_{s,y}$ in Fig. 8(b) retains the same sign on a given side of the wake. One may notice that the two components of the slip velocity vector are of surprisingly similar magnitudes. This is the case because the primary cause of velocity slip is the Kármán vortex cells. A positive slip velocity component in Fig. 8(a) implies that the particles are lagging behind the fluid motion, while $U_{s,x} < 0$ represents particles leading the local fluid. This is fully consistent with the directions of the acceleration vectors on the two sides of the void holes in Fig. 7. The cross-stream slip velocity in Fig. 8(b) is consistently negative in the upper part of the wake ($Y > 0$), i.e. in the direction of negative Y. This reflects that the particles are moving faster towards the centerline in areas where a clockwise vortex gives rise to a negative fluid velocity component $u_y(x_p, t)$. See, for instance in Fig. 7, the densely populated bluish particles just downstream of void hole no 1 which encompasses a clockwise-rotating Kármán vortex. Similarly, we observe that $U_{s,y} > 0$ in the lower part of the wake. We therefore conclude that the cross-stream slip velocity tends to drive all particles towards the symmetry plane $Y = 0$.

### 3.3. Particle trajectories

#### 3.3.1. Group trajectories

Now, after having examined the coherence of the void holes in the cylinder wake, we are shifting our attention to how inertial particles that cluster around a void hole are traveling through the Kármán vortex cells in the near wake. Fig. 9 shows the trajectories of particles landing on both sides of void hole no 2. The coherent voids appear where the first pair of counter-rotating Kármán cells are rolling up and detach from the separated shear layers. We observe from the upper trajectories in Fig. 9 that these particles were first accelerated as they passed the cylinder and the detached shear layer. Most of these trajectories were bent downwards by the first clockwise vortex that shed from the upper shear layer. The particles thereafter experienced a substantial deceleration, caused by an anti-clockwise Kármán vortex shed from the lower shear

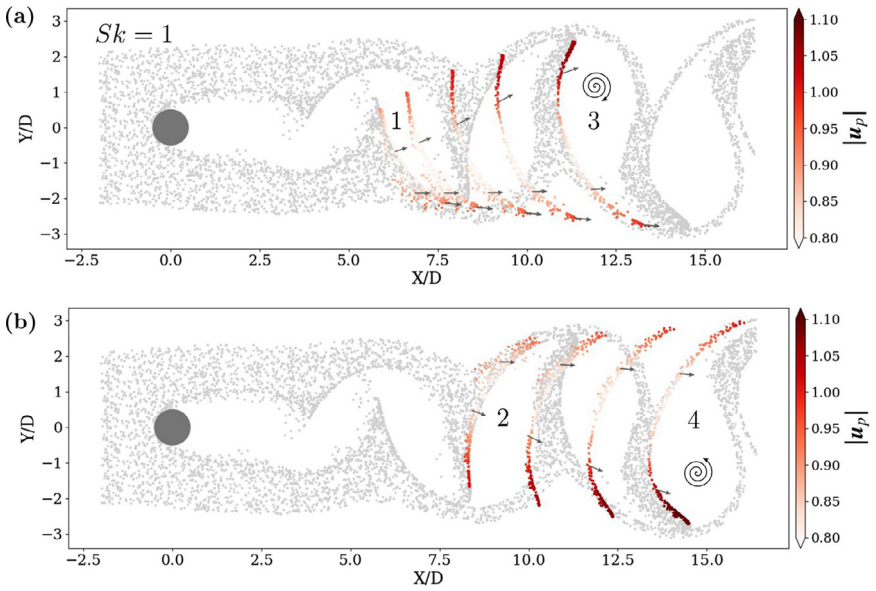


**Fig. 5.** (color online) Backtracking $Sk = 1$ particles that formed the smooth edge of void hole no 3 (a) and void hole no 4 (b) at $t^*$ in time. The backtracked particles are colored by their velocity magnitude $|\boldsymbol{u}_p|$ at time $t^*$, whereas the grey particles are all at $t^*$. The earlier time instants are $T/4$ apart in (a) and separated by $T/3$ in panel (b). The arrows are particle velocity vectors.

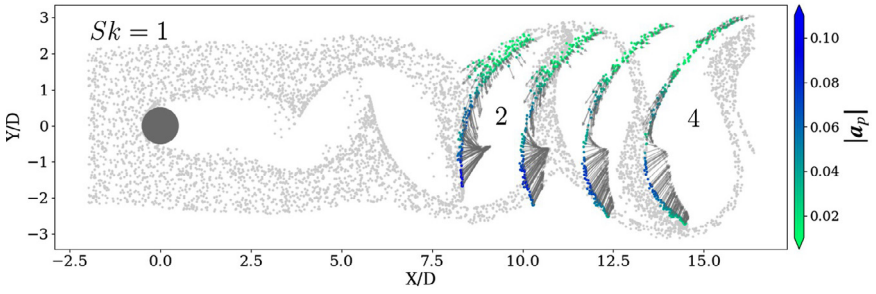


**Fig. 6.** (color online) Backtracking $Sk = 1$ particles that formed the smooth edge of void hole no 4 at $t^*$ in time (same particles as in Fig. 5(b)). The backtracked particles are colored by their acceleration magnitude $|\boldsymbol{a}_p|$ at time $t^*$, whereas the grey particles all are at $t^*$. The earlier time instants are separated by $T/3$ in time. The arrows are particle acceleration vectors.

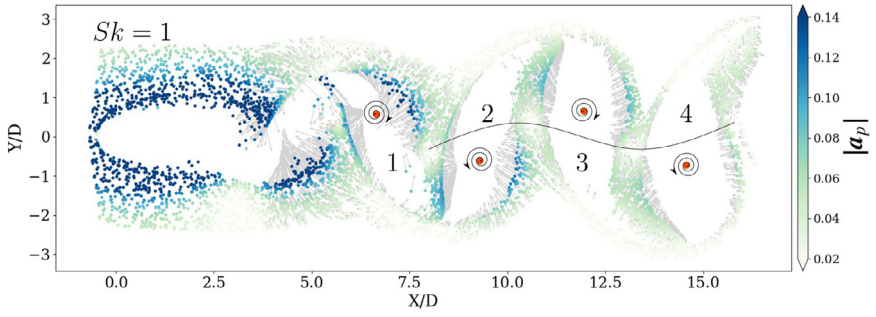


**Fig. 7.** (color online) Particle acceleration $\boldsymbol{a}_p$ at time $t^*$. The point particles are colored according to the magnitude $|\boldsymbol{a}_p|$ and a grey arrow represents the particle acceleration vector. An orange dot shows the position of local maximum of $Q$ in the four vortex cores (embedded in void holes nos 1–4) and the whirls illustrate the sense of fluid rotation.

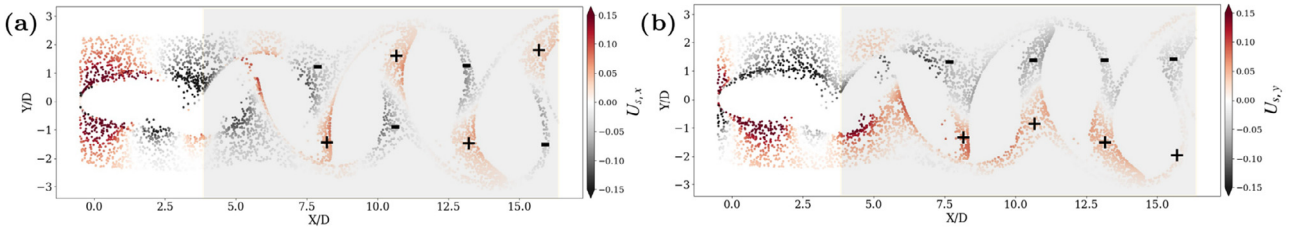


**Fig. 8.** (color online) Slip velocity $\boldsymbol{U}_s = \boldsymbol{u}_{f@p} - \boldsymbol{u}_p$ at time $t^*$. (a) Streamwise component $U_{s,x}$; (b) cross-stream component $U_{s,y}$; '+' and '-' denote areas with positive and negative dominance.

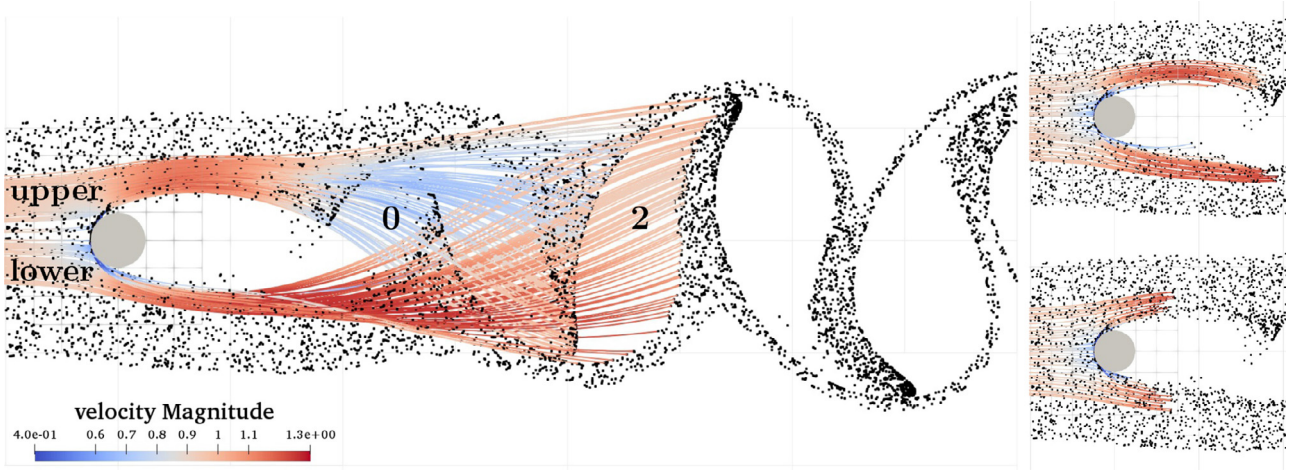


**Fig. 9.** (color online) Left: Trajectories of $Sk = 1$ particles landing on the upstream (smooth) and downstream (blurred) edges of void hole no 2 at time $t^*$, colored by the instantaneous particle velocity magnitude $|\boldsymbol{u}_p|$. The age ranges of particles terminating on upstream and downstream are [18.5, 26.1] and [26.2, 27.3] measured in $D/U_0$, respectively. The age of a particle is defined as the time elapsed since the particle was entered at the inflow boundary. Right: Trajectories of younger $Sk = 1$ particles with ages about $19.8D/U_0$ (upper panel) and $17.8D/U_0$ (lower panel).

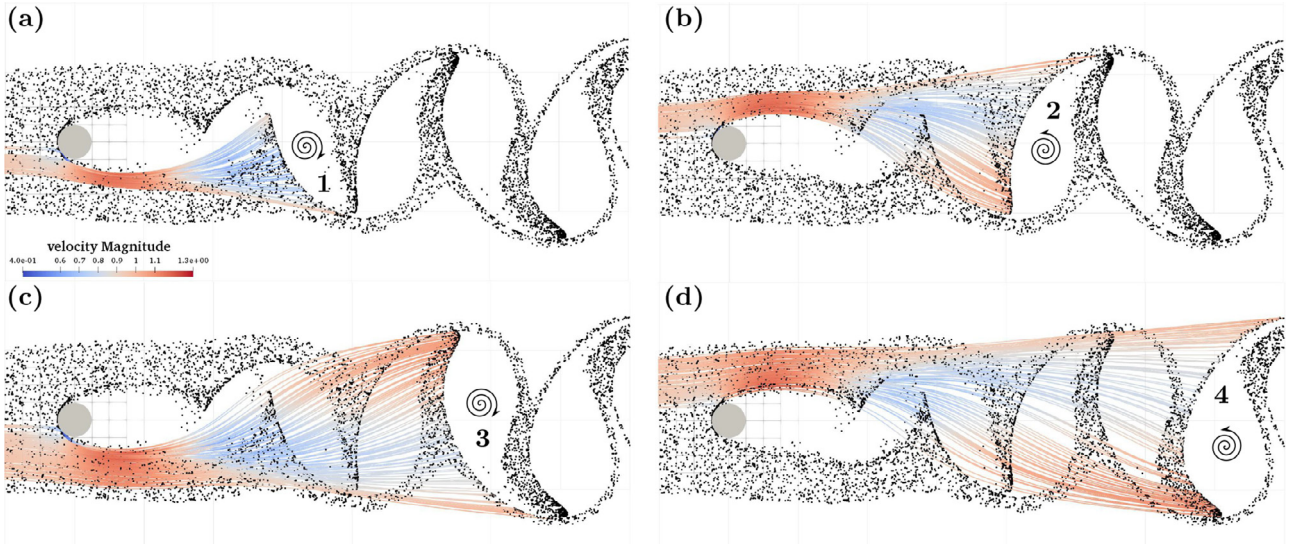


**Fig. 10.** (color online) Trajectories of $Sk = 1$ particles landing on the upstream smooth edge of a coherent void in the wake at time $t^*$. (a) void hole no 1; (b) hole no 2; (c) hole no 3; (d) hole no 4. The black dots show the particle distribution at time $t^*$ and the colors represent the instantaneous particle velocity magnitude $|\boldsymbol{u}_p|$ along the trajectories ranging from 0.4 (blue) to 1.3 (red). The whirls illustrate the sense of vortex rotation. (For interpretation of the references to colour in this figure legend, the reader is referred to the web version of this article.)

layer, before the trajectories reached the smooth edge of void hole no 2 at time $t^*$. In contrast, particles passing below the cylinder maintained their high speed even during the stretch where the upper particles decelerated. Further downstream, however, the lower trajectories are bent upwards due to an anti-clockwise Kármán vortex, but these particles exhibited a more modest deceleration before they ended up at the downstream side of void hole no 2 at time $t^*$. Trajectories of younger particles, i.e. particles injected later than those tracked in the left panel, are shown to the right. As expected, the upper and lower trajectories remain symmetric about the midplane Y = 0 until void hole no 0 is approached. The particle velocity magnitude $|\boldsymbol{u}_p|$ is almost the same at both sides of the near wake until the particles start to be affected by the alternately shed vortex cells.

Next, we focus on group trajectories of the particles clustering at the smooth upstream edge of four different coherent voids at time $t^*$. The colored trajectories in Fig. 10 reveal a non-monotonic variation of the particle velocity $|\boldsymbol{u}_p|$, before the particles end up at the smooth edge of one of the void holes. Similar deceleration periods are seen in each of the four plots. Moreover, the deceleration sets in at roughly the same place in the wake, namely around the location of void hole no 0. This coincides with the position where the separated shear layers are rolling up into Kármán vortex cells; e.g. the formation of the anti-clockwise vortex embedded in void hole no 0 at time $t^*$, as shown in the uppermost plot in Fig. 2. However, the particle deceleration is apparently caused by an oppositely rotating Kármán vortex shed from the other side of the cylinder. This observation is supported by the observation that particles forming the central portion of the smooth edges experienced a longer period with relatively low velocity. Particles terminating near the cusp of the coherent voids are almost unaffected by the counter-rotating Kármán vortices and mostly retain their momentum along the almost straight trajectories. At the particular time instant $t^*$, particles clustering at the smooth edge of an odd-numbered void hole stem from the lower side of the cylinder, whereas those clustered at the upstream edge of even-numbered

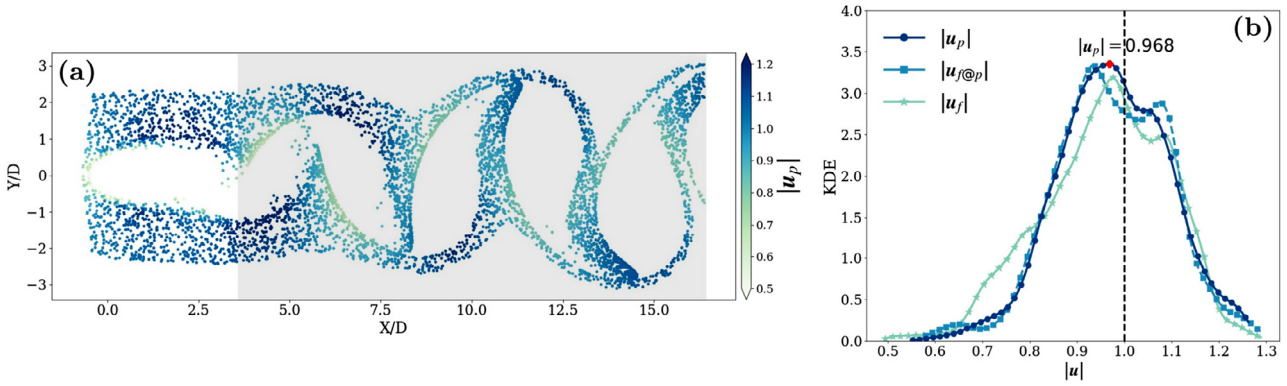


**Fig. 11.** (color online) (a) Particle velocity $\boldsymbol{u}_p$ at time $t^*$. The $Sk = 1$ particles are colored according to the magnitude $|\boldsymbol{u}_p|$; (b) KDE of the particle velocity magnitude $|\boldsymbol{u}_p|$ and the local fluid velocity magnitude $|\boldsymbol{u}_{f@p}|$ based on the particles in the shaded area X = [3.75$D$, 16.5$D$] in panel (a). The red cross denotes the major peak of the KDE of the particle velocity magnitude at $|\boldsymbol{u}_p| \approx 0.968$, whereas the average value is 0.977. (For interpretation of the references to colour in this figure legend, the reader is referred to the web version of this article.)

holes passed above the cylinder. In all cases, however, the trajectories bend towards the mid-plane Y = 0. The deflections of the particle trajectories are caused by the up-rolling vortex that just shed from the separated shear layer. In Fig. 10(a, c), for instance, the bending of the trajectories is due to the anti-clockwise vortex shed from the lower shear layer. As an immediate consequence, the inertial particles are entrained into the central part of the wake. It can finally be seen that the trajectories in Fig. 10(a) look like the first stretches of the trajectories in Fig. 10(c). This confirms the observation made from Fig. 5(a) that particles that clustered at the smooth edge of void hole no 3 could be tracked backwards $T$ in time to coincide with the upstream edge of void hole no 1.

The Lagrangian particle trajectories shown in Fig. 10 revealed that most of the particles that clustered at the upstream smooth edge of one of the coherent voids at time $t^*$ experienced a deceleration period in passing the very-near wake. To examine the imprint, if any, of the particles' history at the present time $t^*$, Fig. 11(a) shows the instantaneous particle velocity magnitude $|\boldsymbol{u}_p|$. Indeed, relatively low velocity magnitudes (greenish particles) are observed for the particles clustered around the smooth edges of the coherent voids. Kernel density estimation (KDE) of $|\boldsymbol{u}_p|$ in Fig. 11(b) exhibits a major peak at $|\boldsymbol{u}_p| = 0.968$, i.e. slightly below the average value 0.977. In contrast, the KDE of the local fluid velocity at the particle positions $|\boldsymbol{u}_{f@p}|$ has two peaks, both of which are separated from the $|\boldsymbol{u}_p|$-peak due to particle inertia.

### 3.3.2. Individual trajectories

The variations of the velocity of particles that cluster at both sides of a void hole seen in Fig. 10 are now explored further by means of trajectories of two particles released at the same time but landing at different sides of void hole no 3. The trajectories of the two particles are plotted in all panels of Fig. 12, to enable comparisons with the streamwise and cross-stream components of the slip velocity, particle velocity and particle acceleration. The coinciding variations of the slip velocity $\boldsymbol{U}_s$ and acceleration $\boldsymbol{a}_p$ components at this Stokes number ($Sk = 1$) suggest that the finite-$Re$ correction factor $\beta$ in Eq. (1) is close to unity.

We observe from Fig. 12(a, c) that both particles are decelerated as they are approaching the cylinder due to the adverse pressure gradient in the stagnation zone. Both particles start to accelerate at X $\approx -0.6D$ and attain maximum acceleration as they pass the shoulders of the cylinder. The particle passing below the cylinder (labeled $P_{low}$) decelerates again already from X $\approx +1.2D$ (light green dot) and is accordingly slowed down severely, until another mild acceleration sets in. The other particle passing above the cylinder (labeled $P_{up}$) experiences a longer acceleration period and accordingly achieves a relatively higher velocity before a stretch of deceleration. The deceleration stage of both particles, caused by the local Kármán vortices, extends over 4–5$D$. The particles are thereafter accelerated once again so that the streamwise particle velocity component $u_{p,x}$ recovers to approximately $U_0$ as the particles land on the respective edges of void hole no 3 at time $t^*$. The particles are now following the fluid more closely and the slip velocity $U_{s,x}$ and the acceleration $a_{p,x}$ are only modestly positive.

Contrary to the decreasing $u_{p,x}$ in front of the cylinder, the magnitude of the cross-stream particle velocity $u_{p,y}$ is rapidly increasing until X $\approx 0$ where a sign-change of $a_{p,y}$ can be observed. Both particles continue to move away from the symmetry plane at Y = 0 for a little while, until $u_{p,y}$ changes sign at X $\approx 2D$. Thereafter, the particle ($P_{low}$) originating at the lower side of the cylinder is dragged by the fluid in the positive Y-direction, whereas the particle ($P_{up}$) passing above the cylinder is dragged in the opposite direction.

## 4. Stokes number effect

After having explored how inertial $Sk = 1$ particles are entrained into the wake and yet leave coherent voids, we finally take a brief look at how particles with higher inertia behave in the same unsteady wake flow. Particles with Stokes number higher than unity are believed to be more weakly coupled to the carrier flow due to their larger inertia. The instantaneous particle concentrations in Fig. 13 show that the more inertial particles are able to penetrate the shear layers that separate from the shoulders of the cylinder and thereafter proceed in the downstream direction relatively unaffected by the alternatingly shed vortex cells, as visualized by color contours of spanwise vorticity $\omega_z$. This leads to the formation of a *void shadow* in the near wake, in contrast to the void cells formed by the $Sk = 1$ particles in Fig. 2. The void shadow extends further downstream with increasing inertia, i.e. higher $Sk$, and thereby postpones the appearance of coherent void cells encompassing the Kármán vortex cells. The increasing particle concentration in high-vorticity regions reflects that the more inertial particles behave ballistically and essentially decouple from the local fluid. The gradually increasing decoupling is caused by the reduction of the factor in front of the slip velocity $\boldsymbol{U}_s$ in Eq. (3). Although coherent voids are formed further downstream in the wake with increasing $Sk$, smooth edges at the upstream side of the void holes can be observed at all Stokes numbers considered. At the downstream side of the voids, however, more particles are dis-

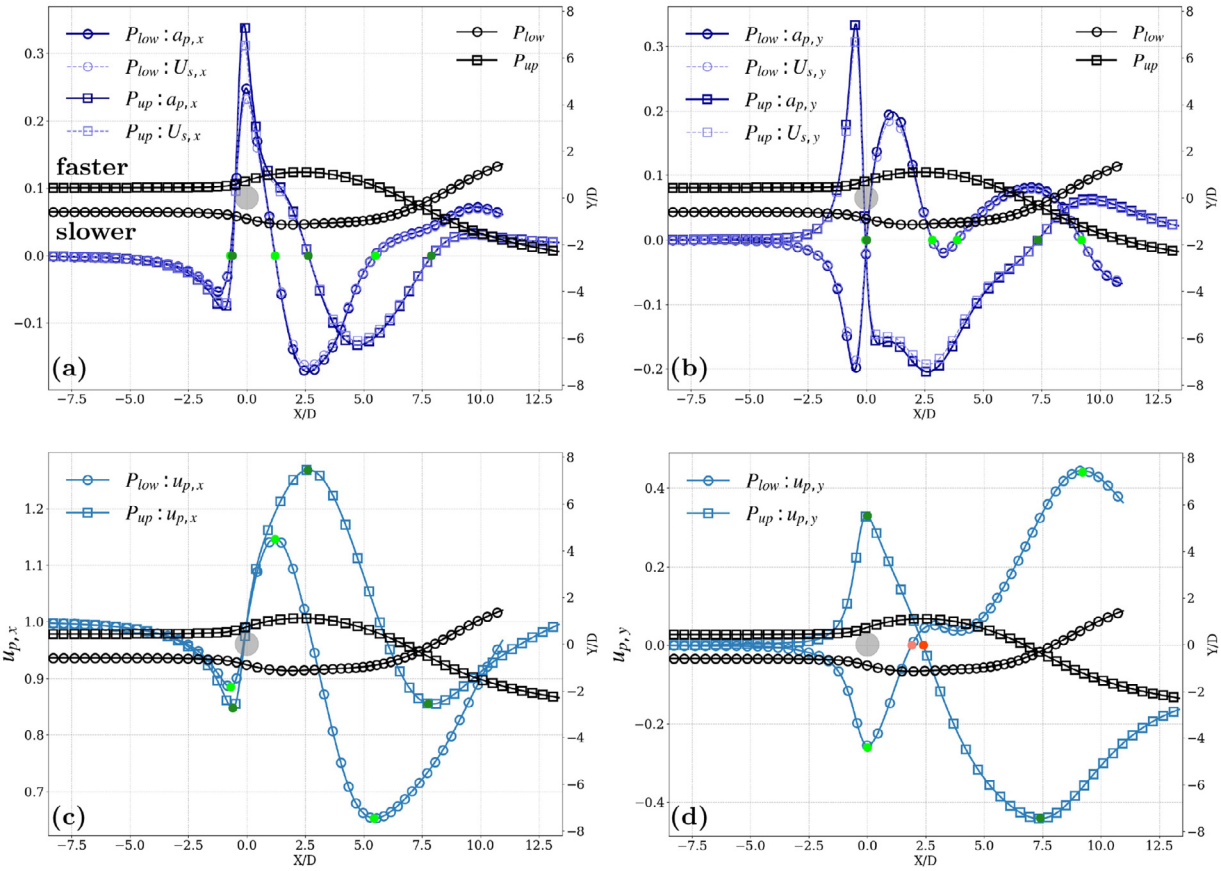


**Fig. 12.** (color online) Trajectories of two different particles landing on the upstream ($P_{low}$, circles) and downstream ($P_{up}$, squares) side of void hole no 3 at time $t^*$ are plotted in all four panels. (a, b) Particle acceleration $\boldsymbol{a}_p$ and slip velocity $\boldsymbol{U}_s$ along the trajectories; (c, d) Particle velocity $\boldsymbol{u}_p$ along the trajectories. Streamwise components are shown in panels (a, c) to the left and cross-stream components in panels (b, d) to the right. The light and dark green dots in (a, c) identify the locations where the streamwise acceleration $a_{p,x}$ of the slow (low) and fast (up) particles changes sign. Similarly, the green dots in (b, d) identify the locations where the cross-stream acceleration $a_{p,y}$ changes sign, whereas the red dots indicate where the cross-stream velocity $u_{p,y}$ changes sign. (For interpretation of the references to colour in this figure legend, the reader is referred to the web version of this article.)

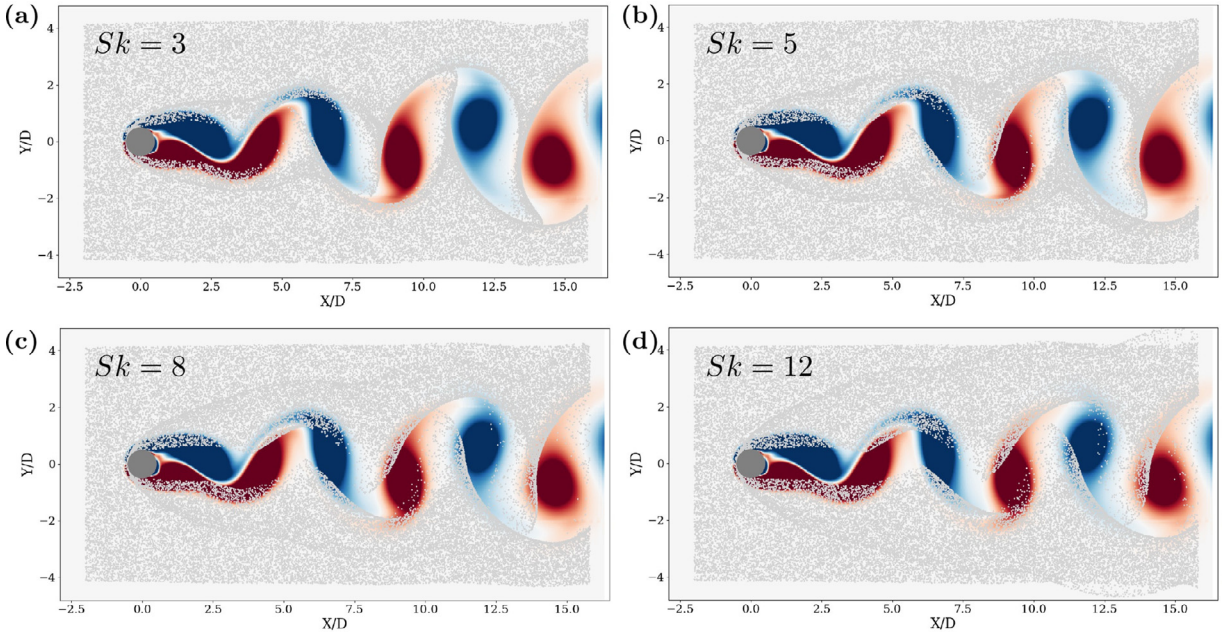


**Fig. 13.** (color online) Instantaneous distribution of heavier particles at time $t^*$ superimposed with the spanwise vorticity $\omega_z$. (a)$Sk = 3$ (b)$Sk = 5$ (c)$Sk = 8$ (d)$Sk = 12$.

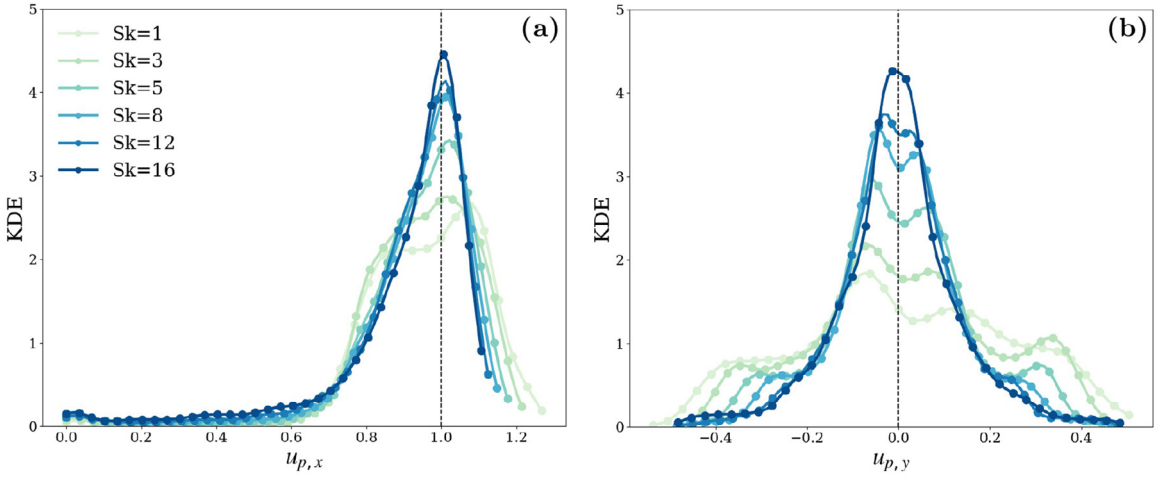


**Fig. 14.** (color online) KDEs of particle velocity at time $t^*$ for six different Stokes numbers. (a)Particle velocity $u_{p,x}$ in the streamwise direction; (b)particle velocity $u_{p,y}$ in the cross-stream direction. Particles are sampled within X $\in [-0.5D, 15.8D]$.

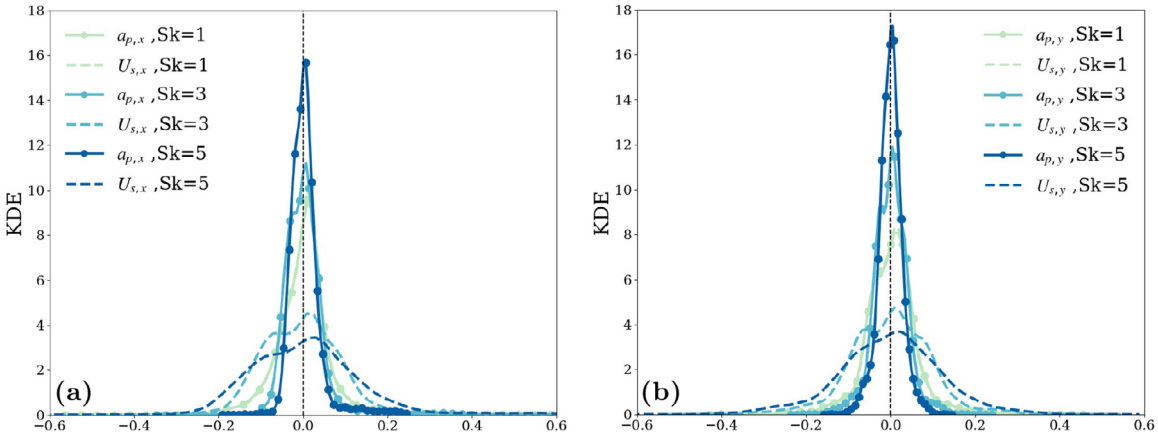


**Fig. 15.** (color online) KDEs of particle acceleration (solid lines) and slip velocity (dashed lines) at time $t^*$ for three different Stokes numbers. (a)$a_{p,x}$ and $U_{s,x}$; (b)$a_{p,y}$ and $U_{s,y}$. Particles are sampled within X $\in [-0.5D, 15.8D]$.

persed around the cusps of the voids, as compared with the clustering of the $Sk = 1$ particles.

In addition to the phenomenological description of the particle concentration patterns in Fig. 13, we also make quantitative comparisons of the instantaneous distributions of the particle velocity, particle acceleration, and slip velocity for some different Stokes numbers to further investigate the effect of particle inertia. The peaks of the six KDEs of the streamwise particle velocity in Fig. 14(a) become higher with increasing inertia while the peak locations monotonically approach the freestream velocity $U_0$. A similarly increasing trend of the central peaks of the KDEs of the cross-stream particle velocity are seen in Fig. 14(b), whereas the secondary peaks at the tails of the KDE-distributions vanish with increasing particle inertia. Particle inertia makes the cross-stream velocity $u_{p,y}$ more concentrated around zero and in particular for the $Sk = 16$ particles for which the two secondary peaks do no longer exist. The left of the two near-by central peaks are consistently higher than the right one. We believe that this is caused by the wake topology at the particular time instant $t^*$, and we conjecture that the right one of the two central peaks will be the higher at $t^* + 1/2T$.

In Fig. 15, the streamwise and cross-stream components of $\boldsymbol{a}_p$ or $\boldsymbol{U}_s$ exhibit fairly similar KDE distributions. However, we observe a significant difference between $a_{p,y}$ and $U_{s,y}$ for the two highest Stokes numbers, namely that the latter is much flatter than that of $a_{p,y}$. With higher inertia most of the particles experience insignificant accelerations in spite of a non-negligible slip velocity. The $Sk = 1$ particles represent an exception, for which the KDEs of the particle acceleration and slip velocity almost coincide, as seen in Fig. 8(c). This suggests that the finite-Re correction $\beta \approx 1$ for the $Sk = 1$ particles, while $\beta$ deviates from unity for higher Stokes numbers in accordance with the semi-empirical correlation in Eq. (2). This explains the decoupling between particle acceleration $\boldsymbol{a}_p$ and slip velocity $\boldsymbol{U}_s$ as an effect of inertia.

## 5. Conclusions

We performed three-dimensional numerical simulations of particle-laden fluid flow around a circular cylinder at $Re = 100$. The unsteady 2D flow is laden with inertial spherical particles characterized by a dimensionless Stokes number ($Sk$). Although previous studies dealt with particle dispersion in cylinder wake flow and/or vortex streets from various aspects, the topology of the particle concentration has never been analyzed in detail, similarly to how we have done in the present manuscript. We focused the investigation on $Sk = 1$ particles, for which it is observed that the inertial particles are expelled from certain parts of the flow field which accordingly appear as *coherent voids*. The local Kármán vortex cells in the near wake contributed to the formation of these voids. Each coherent void encompasses a Kármán vortex shed from the cylinder. An interesting phenomenon is that particles that cluster at the smooth upstream edge of a void hole surrounding a Kármán cell

shed from one side of the cylinder, originate from the other side of the cylinder with oppositely signed vorticity. We could therefore infer that the particles have followed trajectories deflected by a vortex cell shed from the other side. After one shedding period $T$, the smooth edge formed by particles clustering at the circumference of the next void that surrounds a Kármán vortex with the same sense of rotation. In contrast, a few particles are dispersed away from the downstream edge of each void, and this tendency becomes clearer with increasing $Sk$. The lack of experimental data unfortunately disables comparisons with our numerical results. We believe, however, that inclusion of inter-particle collisions naturally occurring in experimental configurations will tend to reduce the sharpness of the edges obtained from numerical simulations.Inter-particle collisions are believed to have only a modest influence on the particle clustering as long as the mass loading is low. Collisions, however, are likely to play a role in particle mixing at larger mass loadings which automatically lead to higher particle-particle collision frequencies.

The centrifugal mechanism is the primary reason for the formation of coherent voids, as shown by means of the $Q$-criterion conditioned on the particle positions. The majority of the particles around the shed vortices are located around the cusps of the vortex cores, while particles in the very near-wake would cast a void shadow which extends further downstream at high $Sk$ as the particles behave more ballistically. However, the pattern formed by the smooth edges is linked to the history of particle movement. We first observed that the instantaneous velocity magnitudes of the particles forming the smooth edges are notably lower than that of the particles downstream of the void holes. This observation suggests that particles originating from different sides of the cylinder are differently affected by one and the same Kármán vortex cell.

The continuous trajectories of particles making up the smooth edges reveal a substantial deceleration period around the first detached shear layer, whereas an acceleration period is simultaneously experienced by the particles dispersed around the downstream edge of the coherent voids. Following a significant deceleration in the near wake, those particles close to the upper/lower parts of the same smooth edges are accelerated by the encompassed vortex core, while the central particles still proceed at lower speed. Therefore, the particles experienced a non-monotonic speed variation along their trajectories. This phenomenon reduces downstream, apparently along with the decaying strength of the vortex cores. The history effect reflected by particle trajectories essentially shapes the smooth edges. The collective effect of particle inertia and path memory could potentially prompt an in-depth examination of the objectivity of aerosol-type flow visualizations from a laboratory perspective, as indicated by Cimbala et al. (1988).

With increasing inertia, i.e. higher $Sk$, the void shadow extends further downstream due to the ballistic movement of the particles. The coherent voids are therefore formed further downstream than in wakes laden with $Sk = 1$ particles. Smooth edges are, however, still observed, although more particles are dispersed away from the downstream edge. Unlike the $Sk = 1$ case, higher particle inertia results in a decoupling of particle acceleration and slip velocity, together with a more inhomogeneous distribution of the instantaneous particle velocity.

Although the particle transportation in 3D turbulent flows appeals to practical applications more than laminar flows, the unsteadiness of dominant large-scale vortex shedding still perseveres. The LSSs in laminar wake flows, to some extent, also persist at high $Re$ in spite of the intense turbulent fluctuations. Therefore, the investigation of particle clustering in the present 2D laminar cylinder wake is believed to share some features with wakes at higher Reynolds numbers.In higher-Re wakes, which inevitably also share some features with HIT, the potential role of other mechanisms, for instance sweep-stick clustering (Goto and Vassilicos 2008), should be explored and their relative importance should be compared with the centrifugal clustering mechanism.

## Declaration of Competing Interest

None.

## CRediT authorship contribution statement

**Zhaoyu Shi:** Software, Validation, Formal analysis, Investigation, Visualization, Data curation, Writing - original draft. **Fengjian Jiang:** Formal analysis, Writing - review & editing. **Lihao Zhao:** Writing - review & editing, Supervision. **Helge I Andersson:** Conceptualization, Writing - review & editing, Supervision, Project administration, Funding acquisition.

## Acknowledgment

The first author greatly appreciates the technical support and guidance on MGLET from Dr. Håkon Strandenes and useful discussions with Dr. Pawel Baj. This work was supported by computational resources provided by Norwegian HPC infrastructure (www.sigma2.no), under project nn2649k granted by Norwegian Research Council. The financial support by NTNU Energy through a research fellowship is appreciated. L.Z. acknowledges the Natural Science Foundation of China (Grant Nos: 11911530141 and 91752205).

## References

Aarnes, J.R., Haugen, N.E.L., Andersson, H.I., 2019. High-order overset grid method for detecting particle impaction on a cylinder in a cross flow. Int. J. Comput. Fluid Dyn. 33, 43–58.
Aliseda, A., Cartlellier, A., Hainaux, F., Lasheras, J.C., 2002. Effect of preferential concentration on the settling velocity of heavy particles in homogeneous isotropic turbulence. J. Fluid Mech. 468, 77–105.
Bagchi, P., Balachandar, S., 2003. Inertial and viscous forces on a rigid sphere in straining flows at moderate Reynolds numbers. J. Fluid Mech. 481, 105–148.
Bagheri, M., Sabzpooshani, M., 2020. On the importance of the history force in dispersion of particles in von Kármán vortex street. Adv. Powd. Tech. 31, 3897–3909.
Bec, J., Biferale, L., Boffetta, G., Celani, A., Cencini, M., Musacchio, S., Toschi, F., 2006. Acceleration statistics of heavy particles in turbulence. J. Fluid Mech. 550, 349–358.
Bec, J., Biferale, L., Boffetta, G., Cencini, M., Musacchio, S., Toschi, F., 2006. Lyapunov exponents of heavy particles in turbulence. Phys. Fluids 18, 091702.
Bec, J., Biferale, L., Cencini, M., Lanotte, A., Musacchio, S., Toshi, F., 2007. Heavy particle concentration in turbulence at dissipative and inertial scales. Phys. Rev. Lett. 98, 084502.
Benczik, I.J., Toroczkai, Z., Tél, T., 2002. Selective sensitivity of open chaotic flows on inertial tracer advection: Catching particles with a stick. Phys. Rev. Lett. 89, 164501.
Bragg, A.D., Collins, L.R., 2014. New insights from comparing statistical theories for inertial particles in turbulence: I. Spatial distribution of particles. New J. Phys. 16, 055013.
Burger, M., Schmehl, R., Koch, R., Wittig, S., Bauer, H.-J., 2006. DNS of droplet-vortex interaction with a Kármán vortex street. Int. J. Heat Fluid Flow 27, 181–191.
Burns, T.J., Davis, R.W., Moore, E.F., 1999. A perturbation study of particle dynamics in a plane wake flow. J. Fluid Mech. 384, 1–26.
Candelier, F., Angilella, J.R., Souhar, M., 2004. On the effect of the Boussinesq-Basset force on the radial migration of a Stokes particle in a vortex. Phys. Fluids 16, 1765–1776.
Cimbala, J.M., Nagib, H.M., Roshko, A., 1988. Large structure in the far wakes of two-dimensional bluff bodies. J. Fluid Mech. 190, 265–298.
Cliff, R., Grace, J., Weber, M.E., 1978. Bubbles, drops, and particles. Academic Press, New York.
Coleman, S.W., Vassilicos, J.C., 2009. A unified sweep-stick mechanism to explain particle clustering in two- and three-dimensional homogeneous, isotropic turbulence. Phys. Fluids 21, 113301.
Daitche, A., Tél, T., 2011. Memory effects are relevant for chaotic advection of inertial particles. Phys. Rev. Lett. 107, 244501.
Daitche, A., Tél, T., 2014. Memory effects in chaotic advection of inertial particles. New J. Phys. 16, 073008.
Dressaire, E., Sauret, A., 2017. Clogging of microfluidic systems. Soft Matter 13, 37–48.
Eaton, J.K., Fessler, J.R., 1994. Preferential concentration of particles by turbulence. Int. J. Multiphase Flow 20, 169–209.
Ferziger, J.H., Tseng, Y.-H., 2003. A ghost-cell immersed boundary method for flow in complex geometry. J. Comput. Phys. 192, 593–623.

Gijs, M.A.M., Lacharme, F., Lehmann, U., 2010. Microfluidic applications of magnetic particles for biological analysis and catalysis. Chem. Rev. 110, 1518–1563.
Gibert, M., Xu, H., Bodenschatz, E., 2012. Where do small, weakly inertial particles go in a turbulent flow? J. Fluid Mech. 698, 160–167.
Gobert, C., 2010. Large Eddy Simulation of Particle-Laden Flow. Technical University of Munich Ph.D. dissertation.
Goto, S., Vassilicos, J.C., 2008. Sweep-stick mechanism of heavy particle clustering in fluid turbulence. Phys. Rev. Lett. 100, 054503.
Haller, G., Sapsis, T., 2008. Where do inertial particles go in fluid flows? Physica D 237, 573–583.
Haugen, N.E.L., Kragset, S., 2010. Particle impaction on a cylinder in a crossflow as function of Stokes and Reynolds numbers. J. Fluid Mech. 661, 239–261.
Hunt, J.C.R., Wray, A.A., Moin, P., 1988. Eddies, streams, and convergence zones in turbulent flows. In: Studying Turbulence Using Numerical Simulation Databases, 2. Proceedings of the 1988 Summer Program. Center for Turbulence Research, Stanford
Ireland, P.J., Bragg, A.D., Collins, L.R., 2016. The effect of Reynolds number on inertial particle dynamics in isotropic turbulence. Part 1. Simulations without gravitational effects. J. Fluid Mech. 796, 617–658.
Jayaram, R., Jie, Y., Zhao, L., Andersson, H.I., 2020. Clustering of inertial spheres in evolving Taylor-Green vortex flow. Phys. Fluids 32, 043306.
Jacobs, G.B., Armstrong, K., 2009. Inertial particle dispersion in the Lagrangian wake of a square cylinder. 47th AIAA Aerospace Sciences Meeting Including the New Horizons Forum and Aerospace Exposition. Orlando
Jung, C., Tél, T., Ziemniak, E., 1993. Application of scattering chaos to particle transport in a hydrodynamical flow. Chaos 32, 555–568.
Kulick, J.D., Fessler, J.R., Eaton, J.K., 1994. Particle response and turbulence modification in fully developed channel flow. J. Fluid Mech. 277, 109–134.
Lee, W., Amini, H., Stone, H.A., Di Carlo, D., 2010. Dynamic self-assembly and control of microfluidic particle crystals. PNAS 107, 22413–22418.
Luo, L., Fan, J., Li, W., Cen, K., 2009. Transient, three-dimensional simulation of particle dispersion in flows around a circular cylinder (Re=140-260). Fuel 88, 1294–1301.
Manhart, M., Friedrich, R., 2002. DNS of a turbulent boundary layer with separation. Int. J. Heat Fluid Flow 23, 572–581.
Manhart, M., Tremblay, F., Friedrich, R., 2001. MGLET: a parallel code for efficient DNS and LES of complex geometries. In: Parallel Computational Fluid Dynamics 2000. Elsevier, Amsterdam, pp. 449–456.
Maxey, M.R., Riley, J.J., 1983. Equation of motion for a small rigid sphere in a nonuniform flow. Phys. Fluids 26, 883–889.
Mohammadreza, M., Bragg, A.D., 2020. Local analysis of the clustering, velocities, and accelerations of particles settling in turbulence. Phys. Rev. Fluids 5, 034306.
Monchaux, R., Bourgoin, M., Cartellier, A., 2010. Preferential concentration of heavy particles: A Voronoï analysis. Phys. Fluids 22, 103304.
Monchaux, R., Bourgoin, M., Cartellier, A., 2012. Analyzing preferential concentration and clustering of inertial particles in turbulence. Int. J. Multiphase Flow 40, 1–18.
Mowlavi, S., Arratia, C., Gallaire, F., 2016. Spatio-temporal stability of the Kámán vortex street and the effect of confinement. J. Fluid Mech. 795, 187–209.
Petersen, A.J., Baker, L., Coletti, F., 2019. Experimental study of inertial particles clustering and settling in homogeneous turbulence. J. Fluid Mech. 864, 925–970.
Raju, N., Meiburg, E., 1997. Dynamics of small, spherical particles in vortical and stagnation point flow fields. Phys. Fluids 9, 299–314.
Salazar, J.P.L.C., De Jong, J., Cao, L., Woodward, S.H., Meng, H., Collins, L.R., 2008. Experimental and numerical investigation of inertial particle clustering in isotropic turbulence. J. Fluid Mech. 600, 245–256.
Shi, Z., Jiang, F., Strandenes, H., Zhao, L., Andersson, H.I., 2020. Bow shock clustering in particle-laden wetted cylinder flow. Int. J. Multiphase Flow 130, 103332.
Squires, K.D., Eaton, J.K., 1991. Preferential concentration of particles by turbulence. Phys. Fluids A 3, 1169–1178.
Tang, L., Wen, F., Yang, Y., Crowe, C.T., Chung, J.N., Troutt, T.R., 1992. Self-organizing particle dispersion mechanism in a plane wake. Phys. Fluids A 4, 2244–2251.
Wang, L., Maxey, M.R., 1993. Settling velocity and concentration distribution of heavy particles in homogeneous isotropic turbulence. J. Fluid Mech. 256, 27–68.
Wen, F., Kamalu, N., Chung, J.N., Crowe, C.T., Troutt, T.R., 1992. Particle dispersion by vortex structures in plane mixing layers. J. Fluids Eng. 114, 657–666.
Yang, Y., Crowe, C.T., Chung, J.N., Troutt, T.R., 2000. Experiments on particle dispersion in a plane wake. Int. J. Multiphase Flow 26, 1583–1607.
Yao, J., Zhao, Y., Hu, G., Fan, J., Cen, K., 2009. Numerical simulation of particle dispersion in the wake of a circular cylinder. Aerosol Sci. Technol. 43, 174–187.
Yoshimoto, H., Goto, S., 2007. Self-similar clustering of inertial particles in homogeneous turbulence. J. Fluid Mech. 577, 275–286.
Zaichik, L.I., Alipchenkov, V.M., 2007. Refinement of the probability density function model for preferential concentration of aerosol particles in isotropic turbulence. Phys. Fluids 19, 113308.
Zhou, H., Mo, G., Cen, K., 2011. Numerical investigation of dispersed gas-solid two-phase flow around a circular cylinder using lattice Boltzmann method. Comput. Fluids 52, 130–138.